Characterization of neoformed illite from hydrothermal experiments at 250 °C and $P_{v,\,soln}$: An HRTEM/ATEM study

Douglas M. Yates* and Philip E. Rosenberg

Department of Geology, Washington State University, Pullman, Washington 99164, U.S.A.

Abstract

Solid products from hydrothermal experiments conducted at 250 °C and $P_{v,soln}$ were characterized by powder X-ray diffraction (XRD) and ATEM/HRTEM. Experiments were conducted with muscovite, kaolinite, and quartz or amorphous silica in 2M KCl solutions for 43 to 176 d. Post-experiment solution compositions lie either within the illite(0.88 K) stability field or on the illite(0.88 K)-kaolinite or illite(0.88 K)-diaspore univariant boundaries in log (a_K^+/a_H^+) vs. log $a_{H_4SiO_4}$ activity space. Transmission electron microscopy (TEM) observations of muscovite grain edges reveal the neoformation of illite crystals with a range of compositions (ATEM) from 0.31 to 0.89 K/$O_{10}(OH)_2$. The range of K-contents appears to narrow toward 0.88 K/$O_{10}(OH)_2$ with increased experiment duration. HRTEM suggests the presence of 2 to 11 layer fundamental particles composed of illitic layers with 10 Å periodicity. Fundamental particle thicknesses increase toward an average of 8 layers/particle with increased experiment duration. In the longer duration experiments, fundamental particle thicknesses were normally distributed about thicknesses of 4 and 8 layers, whereas fundamental particles with thicknesses <4 layers were common in a shorter duration experiment.

The compositions and structure of the illites are consistent with the multiphase model, which states that the smectite-to-illite transition occurs through the step-wise formation of solubility-controlling phases consisting of fundamental particles with thicknesses of 1, 2, 4, and ≥8 layers. The increase in K-content and fundamental particle thickness with the extent of reaction suggests that the illite crystals underwent a prograde reaction culminating in the formation of end-member illite [0.88 K/$O_{10}(OH)_2$]. This reaction, in conjunction with the previously observed, retrograde reaction from muscovite to end-member illite, demonstrates the stability of end-member illite in the system K_2O-Al_2O_3-SiO_2-H_2O at 250 °C.

Introduction

The formation and stability of end-member illite were investigated experimentally in recent studies by Yates and Rosenberg (1996, 1997). These experiments combined muscovite, kaolinite and quartz, or amorphous silica with 2M KCl solutions from 100 to 250 °C to define mica-like, solubility-controlling phases with compositions of 0.29, 0.51, and 0.88 K/$O_{10}(OH)_2$. The experiments at 200 and 250 °C were of particular interest because formation of roughly parallel sets of illite crystals on the edges of altered muscovite grains resulted. The present study characterizes these illites using high resolution transmission electron microscopy (HRTEM) and analytical transmission electron microscopy (ATEM) techniques to gain a better understanding of the smectite-to- end-member illite transition. Goals include determination of solid-state properties, such as composition, structure, and interlayering of illites for which the equilibrating solution compositions are well known.

Nadeau et al. (1984a, 1984b, 1984c) proposed that interstratified I/S is made up of illitic fundamental particles in which the basal interfaces between units behave as smectite interlayers. In this fundamental particle model, smectite, R1 I/S, and R3 I/S are made of populations of discrete fundamental particles with thicknesses of 1, 2, and 4 silicate layers, respectively, whereas end-member illite consists of ≥5-layer fundamental particles. Numerous HRTEM studies of mixed-layer I/S, however, reveal sequences of illitic layers with thicknesses greater than would be predicted by the fundamental particle model (Klimentidis and MacKinnon 1986; Ahn and Peacor 1989; Ahn and Buseck 1990). In an HRTEM study of mixed layer I/S Veblen et al. (1990) observed crystallographic coherence across stacked fundamental particles, including their smectitic interfaces, and suggested that fundamental particles should be redefined as purely illitic units that are coherently stacked within I/S crystallites. Invoking this modified form of the fundamental particle model of Nadeau et al. (1984a, 1984b, 1984c), Rosenberg et al. (1990) proposed a multiphase model for mixed-layer I/S. In this model, the smectite-to-illite transition is

---

* Present address: Department of Geosciences, Princeton University, Princeton, New Jersey 08544. E-mail: yates@geo.princeton.edu

TABLE 1. Experimental data

Exp	Starting materials*	Type†	Duration (days)	pH−pK+	pSiO₂
3219	M-K-Q	solution	84	2.479	2.177
Y202	M-K-Q	solid	43	3.177	2.664
Y203	M-K-A	solid	43	3.350	2.373
3094	M-K-Q	solid	176	3.265	2.630

* M = muscovite, K = kaolinite, Q = quartz, A = amorphous silica.
† Solution or solid equilibration experiment.

thought to occur through the step-wise formation of mica-like phases with compositions of 0.29, 0.51, 0.69, and 0.85–0.88 $K/O_{10}(OH)_2$, which are compositionally analogous to smectite, R1 I/S, R3 I/S, and end-member illite, respectively. Characterization of the illites in the present study should serve as a test of the step-wise nature of the smectite-to-illite transition, as described by the multiphase model.

MATERIALS AND METHODS

Materials

The samples are products of hydrothermal experiments conducted at 250 °C and $P_{v,soln}$ in 2M KCl solutions with Brazilian muscovite, kaolinite and quartz, or amorphous silica (Yates and Rosenberg 1996, 1997). The muscovite starting material is a $2M_1$ polytype with a composition close to end-member muscovite:

$(K_{0.85} Na_{0.08} Ca_{0.02} \square_{0.03}) (Al_{1.88} Fe_{0.08} Mg_{0.05}) (Si_{3.08} Al_{0.92}) O_{10} (OH)_2$.
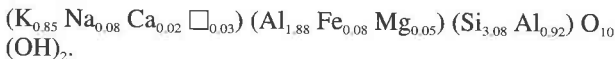
The four samples selected for this study were obtained from two different types of hydrothermal experiments (Table 1).

Powder X-ray diffraction

Solids from the hydrothermal experiments were analyzed by powder X-ray diffraction (XRD) on a Siemens D500 powder XRD using $CuK\alpha$ radiation at 30 mA and 35 kV. Samples were prepared for analysis by lightly grinding under water, followed by deposition of the sample in a thin film on a glass slide. In addition to conventional XRD analyses, the samples were subjected to ethylene glycol solvation using the procedure of Moore and Reynolds (1989). Polytypism was also determined in selected samples using randomly oriented mounts made by passing the samples through a 200 mesh sieve onto a lightly greased glass slide.

Electron microscopy

Sample preparation. Samples were prepared for observation on a Hitachi S570 scanning electron microscope (SEM) by evaporation from water onto carbon coated, 1000 mesh copper grids. The grids were adhered to a high resolution stage with carbon glue and gold coated in a Technics Hummer sputter coater. Samples were prepared for TEM and ATEM by disaggregating the solids in water with a mortar and pestle. Samples were mounted on car-bon-coated, 200 mesh nickel grids by evaporating a drop of the suspended clay slurry with an infrared lamp (Cliff and Lorimer 1975). Some of the prepared grids were coated with a thin layer of gold for use as an internal standard for selected-area electron diffraction (SAED) analyses. A standard consisting of molybdenum oxide crystals was used to account for the relative rotation between SAED patterns and TEM images obtained at selected magnifications. For the HRTEM observations, samples were prepared using the procedure of Lee et al. (1975) in which the sample is sandwiched between 3 mm thick layers of rapid-cure Spurrs epoxy. Prior to application onto the resin, some of the samples were treated with 0.1N dodecylamine hydrochloride (DH) using the intercalation procedure of Ruehlicke and Kohler (1981) to prevent the collapse of smectite layers in the vacuum of the TEM. The epoxy-clay blocks were sectioned using a Reichert ultramicrotome. The ultramicrotome sections were mounted directly onto carbon-coated, 200 mesh copper grids for analysis.

TEM methods. We used a JEOL 1200EX STEM with a Tracor Northern TN5400 energy dispersive spectrometer with a 10 mm² Be window and a Gatan 666 parallel-mounted electron energy loss (EELS) detector. ATEM analyses were conducted at 20–30 Kx in the STEM mode at 12 μA and 120 kV using a variable size raster. Spectra were collected for 100 s analysis time (dead time corrected) while maintaining a 1000 cps input count rate and 30% deadtime with the C1 free-lens control. Background spectra were calculated and subtracted using Desktop Spectrum Analyzer (DTSA) software (National Institute for Standards and Technology). The analyses were conducted with constant instrument settings and count rates for spectra collected from standards and analytes to account for any potassium diffusion under the electron beam (VanDerPluijm et al. 1988).

Compositions of mica-like phases were determined using the thin-film analysis technique of Cliff and Lorimer (1975). Proportionality constants (k-ratios) for each element relative to Si were determined using Wilburne Force hornblende (Al, Ti, Mn, and Fe), Falls Village tremolite (Mg and Ca), Brown Derby Cleavelandite (Na), and Brazilian muscovite (K). After applying a small peak overlap correction, based upon EDS spectra collected from the Brazilian muscovite standard, peak integrals were converted to oxide weight percents using the k-ratios and normalized to 100%. The oxide weight percent values were then recalculated on the basis of 11 O atoms and the tetrahedral and octahedral site ions were normalized to six ions. The normalization factor was used as a test of the quality of the analysis; analyses requiring a normalization factor, which deviated from 1 by more than 0.02 were discarded. Using this analysis procedure, Yates (1993) showed that I_K/I_{Si} ratio of the Brazilian muscovite standard is independent of both relative grain thickness, determined by EELS, and analysis time. These observations suggest that analyses are not influenced by the ef-
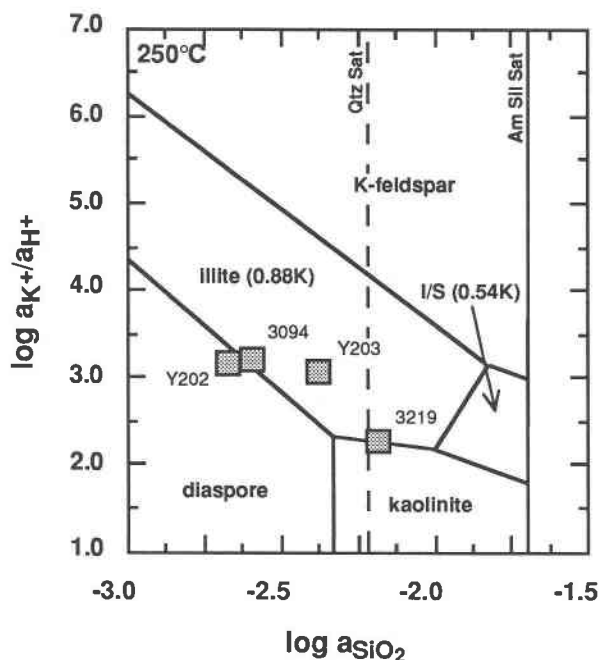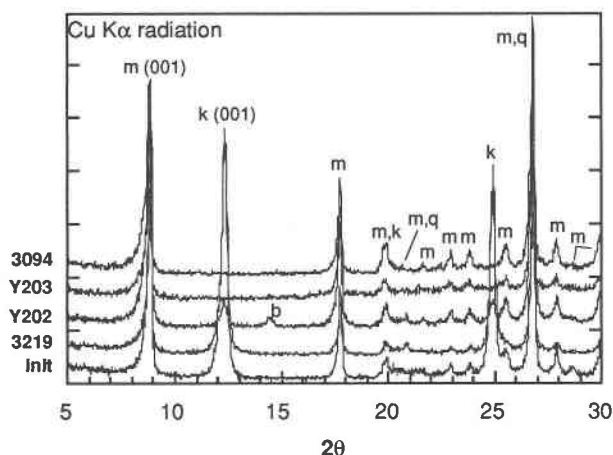
FIGURE 1. Isothermal, isobaric log (a_K^+/a_H^+) vs. log a_{H4SiO4} activity diagram showing solution compositions (shaded squares) from hydrothermal experiments with muscovite, kaolinite and quartz, or amorphous silica. Univariant boundaries defining the stability field of mica-like phases are from Yates and Rosenberg (1996). Quartz and amorphous silica saturation limits are from Walther and Helgeson (1977).

FIGURE 2. Powder X-ray diffractograms obtained from a mixture of the muscovite and kaolinite starting materials (init) and from the products of the experiments. Reflections of muscovite (m), kaolinite (k), quartz (q), and boehmite (b) are labeled.

fects of potassium boil-off or potassium diffusion described by VanDerPluijm et al. (1988) and Peacor (1992).

HRTEM observations. One-dimensional lattice fringe images were recorded using (00*l*) reflections at magnifications of 100 to 300 Kx. A through-focus series was taken starting from an over focus of $\Delta f = +300$ Å to an under focus of $\Delta f = -1500$ Å in 300 Å steps. The one-dimensional lattice fringe images of illite at Scherzer focus (Spence 1981) consist of dark and thick, light fringes that are inferred to represent tetrahedral layers and interlayer sites, respectively, as similar images do in the HRTEM simulations of muscovite (Guthrie and Veblen 1990). Thicknesses of mica-like particles were measured by counting the number of tetrahedral sheets (dark fringes) in each particle. This measurement corresponds to the thickness of the particles, measured in nanometers (nm), because the tetrahedral sheets in the muscovite (or illite) structure are separated by 1 nm.

CHARACTERIZATION

The post-experiment solution compositions (Fig. 1) are closely related to the observed solid assemblages (Fig. 2). The solution composition from Experiment 3219 lies on the illite(0.88 K)-kaolinite boundary at quartz saturation. This solution composition is consistent with the equilibration of the synthetic illite with kaolinite and quartz starting materials. In Experiments Y203 and 3094 the dis-
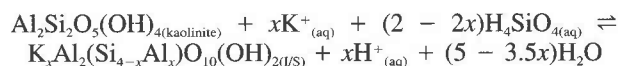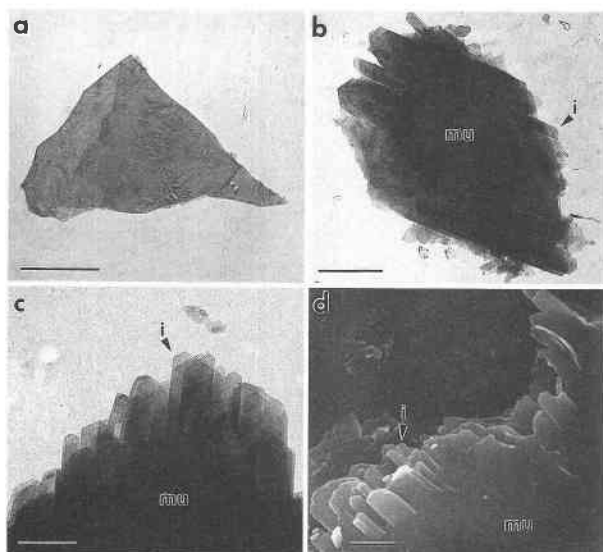
solution of kaolinite (Fig. 2) led to solution compositions within the divariant illite(0.88 K) field and on the illite(0.88 K)-diaspore boundary, respectively. The identification of boehmite in Experiment Y202 (Fig. 2) may explain solution compositions from this experiment and that of 3094, which lie on the illite(0.88 K)-diaspore boundary. Inasmuch as the illite(0.88 K)-boehmite and illite(0.88 K)-diaspore boundaries are nearly coincident in log (a_K^+/a_H^+) vs. log a_{H4SiO4} activity space (Yates and Rosenberg 1996), the assemblage illite(0.88 K)-boehmite may be expected to equilibrate near the illite(0.88 K)-diaspore boundary in the absence of quartz.

XRD analyses indicate a lack of structural changes in the muscovite starting materials during equilibration (Fig. 2). None of the peaks that are diagnostic for the $1M_d$ and $1M$ polytypes (Bailey 1984) were observed in patterns collected from the experimental samples. Ethylene glycol solvation of the samples yielded XRD patterns with an average $\Delta 2\theta$ parameter (Środoń 1980) of 8.99(3), which is characteristic of 0% expandable illite. These observations suggest that either the synthetic illites produced in the experiments have identical structures to that of the muscovite starting material (i.e., $2M_1$ polytype, 0% expandable) or that the illite crystals represent too small a fraction of the sample to be detectable by XRD.

A comparison of the kaolinite (001) peak intensities in the starting material-mixtures with those of the products (Fig. 2) indicate the partial dissolution of kaolinite in Experiments 3219 and Y202 and total or near total dissolution in Experiments Y203 and 3094. The dissolution of kaolinite during equilibration suggests that the precipitation and growth of the neoformed illites occurred by a reaction that consumed kaolinite, such as:

$$Al_2Si_2O_5(OH)_{4(kaolinite)} + xK^+_{(aq)} + (2 - 2x)H_4SiO_{4(aq)} \rightleftharpoons$$
$$K_xAl_2(Si_{4-x}Al_x)O_{10}(OH)_{2(I/S)} + xH^+_{(aq)} + (5 - 3.5x)H_2O$$

where x is the K-content of I/S. XRD analyses and TEM

FIGURE 3. Transmission and scanning electron micrographs of the muscovite starting material and products from Experiment Y203. (**a**) A transmission electron micrograph of the muscovite starting material (scale bar = 2.0 μm). (**b** and **c**) Transmission electron micrographs of muscovite (mu) grains with neoformed illite (i) crystals [scale bar = 1.0 μm (**b**) and 0.25 μm (**c**)]. (**d**) A scanning electron micrograph of a muscovite grain edge with neoformed illite crystals (scale bar = 1.0 μm).

FIGURE 4. (**a**) Transmission electron micrograph of illite crystals (arrow heads) on a muscovite (mu) grain edge from Experiment Y203 (scale bar = 0.5 μm). (**b** to **d**) Selected-area diffraction patterns of the (001) plane of the muscovite grain (**b**), a single illite crystal [left arrow in (a)] (**c**) and several illite crystals [right arrow in (a)] (**d**). Arrows on the SAED patterns indicate the a* axis.
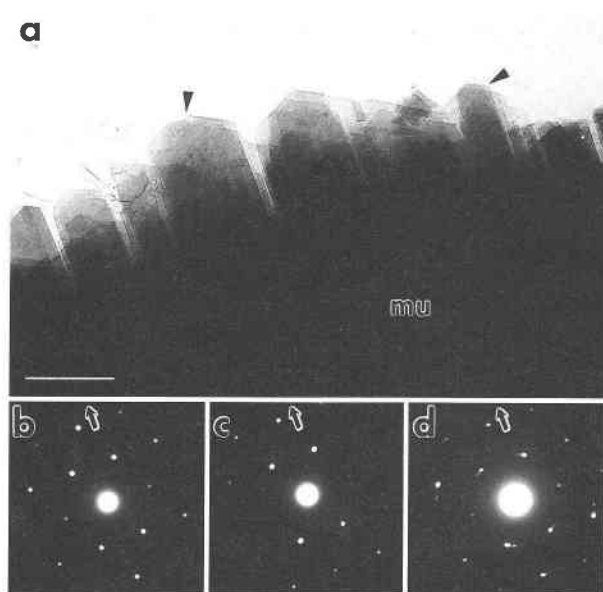
observations (see following section) show, however, that quartz and muscovite also underwent partial dissolution during equilibration, providing some of the SiO_2 (aq) and K^+ necessary for illite precipitation.

Transmission electron microscopy observations

TEM images show that the muscovite starting material consists of subhedral grains (0.5 to 5.0 μm) with smooth, unaltered edges (Fig. 3a). Images of post-experiment solids (Figs. 3b–3d), however, reveal that a reaction has taken place resulting in the formation of illite laths at muscovite grain edges. The laths range in size from 0.2 to 1.0 μm wide by 0.1 to 2.0 μm long. The illite crystals appear well formed with triangular terminations and are arranged on the muscovite grain edges in parallel groups of 2 to >10 crystals (Figs. 3c–3d).

The extent of illitization and muscovite grain alteration increases in the order: 3219 < Y202 ≈ Y203 < 3094. The extent of illitization appears to be proportional to the extent of kaolinite dissolution in these samples as determined by XRD (Fig. 1). The extent of illitization is not, however, determined solely by experiment durations (Table 1). Although Experiment 3219 was conducted for a longer duration than Experiments Y202 and Y203, the low solution-to-solid ratio used in Experiment 3219 apparently slowed the rate of the illitization reaction. Thus, owing to the differences in the solution-to-solid ratios in the experiments, the durations of experiments, listed in Table 1, do not necessarily reflect the extent of reaction.

SAED patterns of the muscovite (001) planes (Fig. 4) were indexed in accordance with the $2M_1$ polytype (space group, $C2/c$) (Güven 1974). The SAED patterns of the illite crystals were indexed assuming an identical crystallographic orientation as that of the muscovite grain to which they were attached. Measurements taken from the SAED patterns of the illite crystals yielded lattice parameters of a = 5.17(3) and b = 9.00(4) Å. The absence of $hk0$ rings in the SAED patterns of the illites indicates that the stacking of silicate layers is non-turbostratic (Veblen et al. 1990), although some SAED patterns revealed some circular streaking of spots probably arising from several stacked illite crystals with nearly parallel orientation (Fig. 3d). Comparison of the TEM image (Fig. 4a) and the SAED pattern obtained from the muscovite grain (Fig. 4b), shows that the illite laths grew parallel to the [200]*, and less commonly, the [$\bar{3}$10]* directions of the muscovite substrate. The [200]* and [$\bar{3}$10]* directions of the reciprocal lattice correspond approximately to the [100] and [$\bar{1}$10] directions in the direct lattice, respectively.

Analytical transmission electron microscopy

Compositions of individual illite crystals from each of the experiments are given in Table 2. The low Mg-content of the illites allows their compositions to be represented in terms of Si/4 ratios vs. alkali-site occupancy (Figs. 5a–5d). The coordinate, Si/4, is useful because the value of Si/4 is inversely proportional to the silicate-layer charge in an R^{2+}-free illite. The compositions indicated for I/S with selected thicknesses refer to predictions made on the basis of the multiphase model (see later discussion).

TABLE 2. Average compositions of illites

Exp	Si	ivAl	viAl	Fe	Mg	Ca	Na	K	Alk*	Number†
3219‡	3.44	0.56	1.98	0.02	0.00	0.01	0.03	0.33	0.39	11
esd	0.05	0.05	0.02	0.02	0.00	0.01	0.04	0.06	0.05	
3219‡	3.26	0.74	1.98	0.01	0.01	0.01	0.06	0.60	0.68	13
esd	0.09	0.09	0.03	0.02	0.02	0.02	0.05	0.10	0.09	
Y202	3.21	0.79	1.99	0.01	0.00	0.00	0.01	0.71	0.73	43
esd	0.06	0.06	0.01	0.01	0.01	0.01	0.02	0.08	0.08	
Y203	3.20	0.80	1.99	0.00	0.01	0.00	0.01	0.72	0.73	40
esd	0.05	0.05	0.03	0.01	0.03	0.00	0.02	0.08	0.08	
3094	3.19	0.81	1.96	0.04	0.00	0.02	0.03	0.70	0.79	19
esd	0.04	0.04	0.03	0.03	0.00	0.03	0.05	0.07	0.04	

* Alkali-site occupancy.
† Number of analyses.
‡ Bimodal averages (statistically different at 99% confidence level in terms of alkali-site occupancy and Si-content).

Although the illites exhibit a wide range of alkali-site occupancies (Fig. 5), the ranges of alkali-site occupancies narrow from 0.31–0.89 $K/O_{10}(OH)_2$ in Experiment 3219 to 0.72–0.87 $K/O_{10}(OH)_2$ in Experiment 3094. Illites from Experiments Y202 and Y203 have an intermediate range of alkali-site occupancies from approximately 0.50 to 0.89 $K/O_{10}(OH)_2$. It is interesting that Experiment 3219 possesses two groups of illite compositions. The group with lower K-content has an average alkali-site occupancy of 0.39(5) $K/O_{10}(OH)_2$, whereas the group with higher K-content has an average alkali-site occupancy of 0.68(9)/$O_{10}(OH)_2$. The higher-K illites from Experiment 3219 exhibit K-contents similar to those from Experiments Y202 and Y203, which have average compositions of 0.73(8) $K/O_{10}(OH)_2$. Analyses of Experiment 3094 revealed the highest observed K-contents with an average alkali-site occupancy of 0.79(4) $K/O_{10}(OH)_2$. An increase in the tetrahedral site charge accompanies increasing alkali-site occupancies in the experiments, due to an Al^{3+} for Si^{4+} substitution.

The increasing alkali-site occupancies obtained for illites formed in these respective experiments support the trend in the extent of reaction and illite growth in the order: 3219 < Y202 ≈ Y203 < 3094 (Table 2) observed by TEM. Therefore, illite compositions in the experiments appear to be evolving toward an alkali-site occupancy of ~0.88 $K/O_{10}(OH)_2$, the average upper limit observed in the experiments.

High resolution transmission electron microscopy

One-dimensional lattice-fringe images show that the muscovite starting material consists of particles having thicknesses of 15 to 100 layers with few defects or layer terminations (Fig. 6a). In a majority of the HRTEM images of the muscovite, single silicate layers could be traced across the entire length of the crystal. In a few places, the interlayer spacing of 10 Å is superimposed on a 20 Å spacing, characteristic of the $2M_1$ polytype structure of the muscovite starting material (Fig. 6c). Many of the HRTEM images of the muscovite revealed a mottled contrast (Fig. 6a). Jiang et al. (1990) attributed this con-
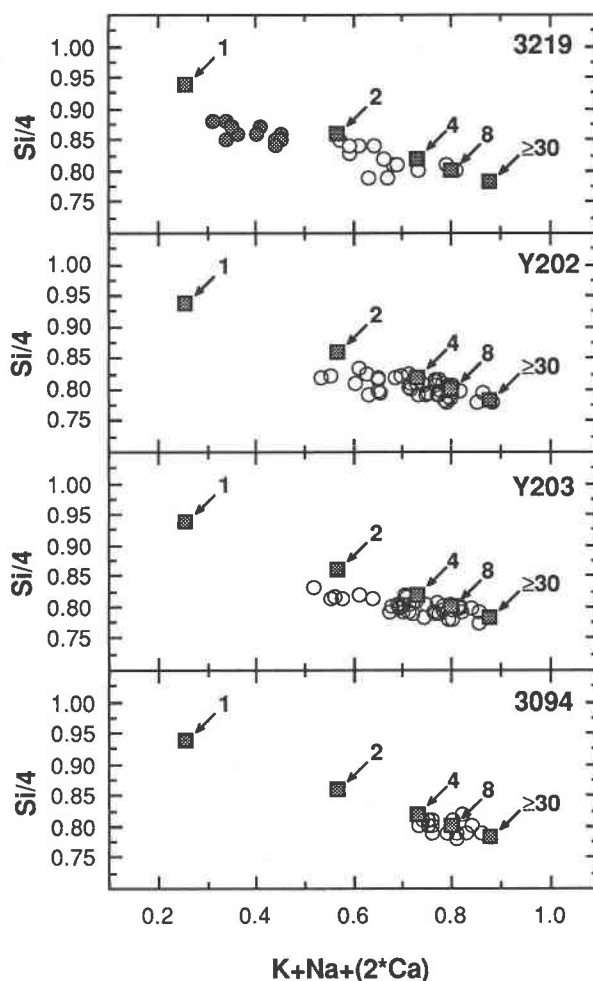

FIGURE 5. Si/4 vs. alkali-site occupancy diagram showing individual ATEM analyses of synthetic illite crystals (circles) formed in the experiments. A bimodal distribution of compositions in Experiment 3219 is indicated by shaded vs. open symbols. Square symbols represent the calculated composition for mica-like phases consisting of the indicated number of silicate layers, discussed below.

trast to be some kind of strain phenomenon, which may be partially caused by cation diffusion during irradiation by the electron beam of the TEM.

In untreated experimental samples, the thicknesses of the synthetic illite crystals varied from approximately 40 to 300 Å. The illites occur as stacks of crystals merging to form thicker aggregates identical to that of the adjacent muscovite substrate (Fig. 6b). Examination of HRTEM images failed to reveal specific nucleation sites for the illite crystals on the muscovite substrate. This observation suggests that epitaxial growth of illite on muscovite may be promoted by dissolution along planes of weakness normal to the (001) crystallographic plane of the muscovite structure, thereby forming a lath-like morphology. This mechanism is supported by SAED observations of synthetic illite growth nearly parallel to the [$\bar{1}$10] crystallo-
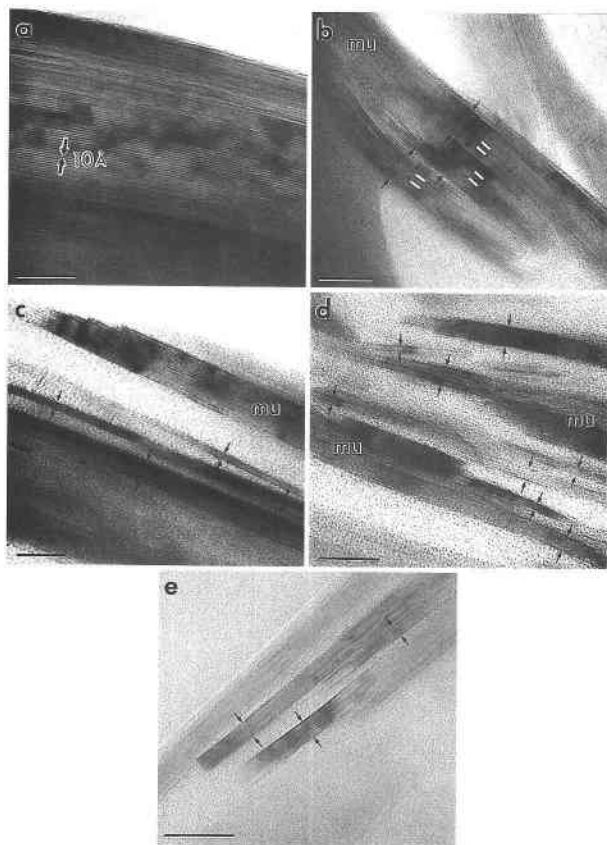
FIGURE 6. One-dimensional lattice fringe images. (a) The muscovite starting material showing a typically thick grain with 10 Å layering ($\Delta f \cong -1200$ Å). (b) An untreated sample from Experiment Y203 showing illite crystals (arrows mark cross sections) on muscovite (mu) grain edges. Wide, dark fringes (white bars) may occur near smectite layers ($\Delta f \cong +300$ Å). (c to e) DH treated samples from Experiments 3219 (c), Y203 (d) and 3094 (e) showing illite fundamental particles (arrows mark cross sections) on or near muscovite (mu) grains.

graphic direction of the muscovite substrate, which is parallel to a plane of structural weakness in muscovite (Jasmund et al. 1969; Güven 1972).

Examination of overfocused lattice images of individual illite crystals (Fig. 6b), reveals the presence of subunits of 2 to >8 layers separated by thicker, dark fringes. The thicker, dark fringes may represent smectite interlayers in the I/S crystallite (Guthrie and Veblen 1989), and thus, the illitic units may be considered fundamental particles. As was discussed earlier, SAED patterns collected from the individual illite crystals revealed little evidence of turbostratic stacking (Fig. 3c). Therefore, the illite crystals appear to consist of crystallographically coherent stacks of purely illitic fundamental particles. This conclusion is supported by the HRTEM observations of Veblen at al. (1990) that indicate that fundamental particles occur within I/S crystallites as nonturbostratic, coherent stacks, separated by smectite interlayers.

Fundamental particle thicknesses

The intercalation treatment resulted in the partial or complete disarticulation of the illite crystals, due to infinite swelling along smectite interlayers (Figs. 6c–6e). Examination of the disarticulated particles reveals 10 Å layering with no evidence of smectitic interlayers, which may be detected by over-focused HRTEM images (Guthrie and Veblen 1989). Therefore, the particles produced as a result of the DH treatment, are assumed to be fundamental particles.

The fundamental particle thicknesses increase in the order 3219 < Y203 < 3094 (Fig. 7, Table 3). The observed increase in average fundamental particle thickness from 3.5 layers/particle in Experiment 3219 to 5.2 and 6.4 layers/particle in Experiments Y203 and 3094, respectively, corresponds directly to the compositional trends observed in these experiments (Figs. 5a, 5c, and 5d). If it is assumed that the fundamental particles possess high-K interlayers and relatively lower-K basal edges (smectitic interlayers) then the increase observed in alkali-site occupancies is due to increases in fundamental particle thicknesses.

Particle thicknesses determined for Experiment Y203 in the range of 2–8 layers/particle are normally distributed (at 95% confidence level) around a particle thickness of 4.3 layers/particle. Likewise, fundamental particle thicknesses indicated for Experiment 3094 are bimodally distributed (at 95% confidence level) around particle thicknesses of 4.5 and 8.3 layers. Thus, the fundamental particle thicknesses determined for Experiment Y203 and 3094 appear to be normally distributed around thicknesses of approximately 4 and 8 layers. The distribution of particle thicknesses in illites from Experiment 3219 is not as well defined as those for experiments of longer duration, although fundamental particle thicknesses of ≤4 layers were more commonly observed. The lack of a well defined distribution of particle thicknesses in Experiment 3219 may be due to the low solution-to-solid ratio used in this experiment, which had the effect of decreasing the extent of reaction.

DISCUSSION

Correlation of composition and structure: multiphase model

Discrete solubility-controlling phases with compositions of 0.29, 0.51, 0.69, and 0.85–0.88 K/O$_{10}$(OH)$_2$ were inferred in the products of previous hydrothermal experiments with muscovite or illite starting materials (Aja et al. 1991; Aja 1991; Yates and Rosenberg 1996). According to the multiphase model (Rosenberg et al. 1990), these solubility-controlling phases consist of fundamental particles with thicknesses of 1, 2, 4, and ≥8 silicate layers, respectively (Fig. 8). The fundamental particles consist of stacks of illitic layers and are bounded by smectitic basal surfaces (Nadeau et al. 1984a, 1984b, 1984c). Unlike the original fundamental particle model presented by Nadeau et al. (1984a, 1984b, 1984c), we believe that the
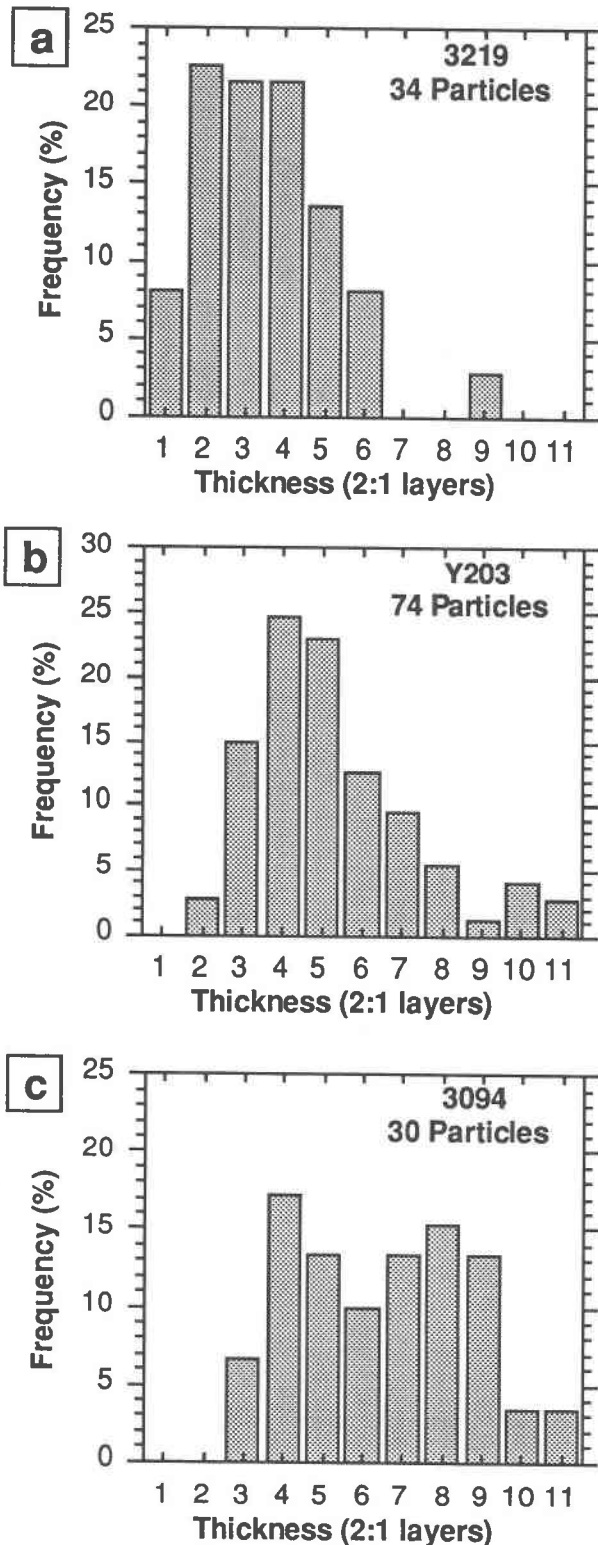
TABLE 3. Measurements from lattice fringe images

Sample number	Number fundamental particles measured	Total silicate layers	Silicate layers per particle
3219	34	127	3.5 ± 1.7
Y203	74	388	5.2 ± 2.0
3094 (all)	30	193	6.4 ± 2.2
3094 (group 1)*	15	68	4.5 ± 1.0
3094 (group 2)*	15	125	8.3 ± 1.2

* Bimodal distribution (statistically different at 95% confidence level).

fundamental particles occur as units of larger, crystallographically coherent I/S crystallites (Veblen et al. 1990; present study), rather than as discrete, turbostratically stacked particles.

Idealized compositions were derived for smectite, R1 I/S, R3 I/S, and end-member illite (Fig. 8) by assuming these phases consist of fundamental particles with thicknesses of 1, 2, 4, and 8 to ≥30 layers, respectively, with smectitic basal surfaces (Rosenberg et al. 1990). The compositions reflect an illite layer composition of $0.88 K/O_{10}(OH)_2$, whereas the smectite layers are assumed to have a composition of $0.25 K/O_{10}(OH)_2$. It is further assumed that the silicate sheets adjacent to the edges of the fundamental particles have a lower charge than the silicate sheets bounding illitic layers within the fundamental particles. This difference in layer charge accounts for the lower alkali-site occupancy at the basal surfaces. In an R^{2+}-free stoichiometry, close to that of the illites formed
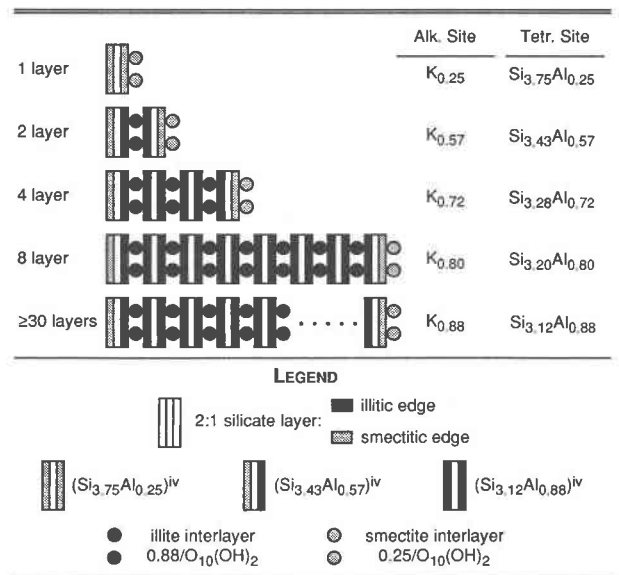

FIGURE 7. Histograms showing the relative frequency of fundamental particle thicknesses (number of silicate layers) measured from lattice fringe images of DH treated illites formed in hydrothermal experiments at 250 °C. Total number of measured particles is indicated for each sample.

FIGURE 8. Schematic diagram showing the basic structural units for 1, 2, 4, 8, and ≥30 layer fundamental particles. Compositions (in an R^{2+}-free structure) of the fundamental particles and their components are indicated in terms of alkali- and tetrahedral site occupancies.

in the present study, the decreased charge in layers adjacent to the basal surfaces is due to substitution of Si^{4+} for Al^{3+} in the tetrahedral site. Fundamental particles with ≥ 30 layers were included in Figure 8 to represent illite with infinitely thick fundamental particles, whereas the fundamental particles with ≥ 8 layers represent the broad class of low expandability illites with K-contents from 0.80 to 0.89 $K/O_{10}(OH)_2$ (e.g., San Juan sericites, Eberl et al. 1987).

Using the compositions derived for the fundamental particles (Fig. 8), it is possible to relate the compositions of the illites to fundamental particle thicknesses observed by HRTEM (Fig. 7). Compositions corresponding to those derived by the multiphase model are indicated in Figure 5. The bimodal distribution of compositions exhibited by sample 3219 (Fig. 5a) appears to represent two groups of illites with differing particle thicknesses. The group with low K-content is consistent with a mixture of one and two layer fundamental particles, whereas the higher-K group suggests the presence of two to four layer fundamental particles, as well as several crystals with ~8 layer particles. Experiments Y202 and Y203 (Figs. 5b and 5c) appear to contain fundamental particle thicknesses ranging from 2 to ≥ 8 layers, whereas sample 3094 has illite compositions consistent with 4 to ≥ 8 layer fundamental particles.

Predictions of fundamental particle thicknesses based upon the multiphase model are generally supported by the thicknesses of fundamental particles observed by HRTEM (Fig. 7). However, it is clear from the range of alkali-site occupancies exhibited by the illites (Fig. 5), that the observed compositions do not conform to the exact compositions predicted by the multiphase model (Fig. 8). This discrepancy is due, in part, to the nature of the HRTEM vs. ATEM observations. While the HRTEM images of the DH treated samples reveal the thicknesses of individual fundamental particles, ATEM analyses of the illite crystals yield average compositions of aggregates of three or more fundamental particles (e.g., Fig. 6b). Therefore, the presence of fundamental particles with differing thicknesses within individual illite crystals may contribute to the range of observed illite compositions.

The fundamental particles exhibit a range of thicknesses other than those of 1, 2, 4, and ≥ 8 layers (Fig. 7). As is the case in natural sequences of I/S (e.g., Eberl 1993; Inoue et al. 1987), a seemingly continuous series of illite compositions marks the prograde illitization reaction in the experiments (Fig. 5). However, the illite crystals appear to consist of fundamental particles with thicknesses that are normally distributed about 2, 4, and ≥ 8 layers. Therefore, fundamental particles with thicknesses other than those predicted by the multiphase model, may account for the apparently continuous increases observed in K-content.

In a recent HRTEM study of diagenetic and hydrothermally formed smectites and illites, Dong et al. (1997) observed the prograde sequence: smectite $\rightarrow$ R1 I/S $\rightarrow$ illite. HRTEM observations confirmed that the smectite

and R1 I/S phases consisted of one and two layer fundamental particles, respectively, whereas the illite consisted of thick stacks of illitic layers with few smectitic interlayers. These phases are closely analogous to mica-like phases consisting of 1, 2, and ≥ 8 layers inferred by the multiphase model (Fig. 8). Dong et al. (1997) also noted that mixed-layer phases with I/S ratios between those of smectite, R1 I/S, and illite were present only in minor amounts. Aside from the absence of R3 I/S (ISII), the observations of Dong et al. (1997) are consistent with the step-wise formation of mica-like phases (smectite $\rightarrow$ R1 I/S $\rightarrow$ R3 I/S $\rightarrow$ end-member illite) proposed by the multiphase model.

Therefore, we believe that the smectite-to-illite transition occurs through a step-wise reaction from smectite (one layer particles) to I/S with two and four layer particles, culminating with the formation of end-member illite with ≥ 8 layers fundamental particles. Each of the "steps" encountered in this transition represents a phase consisting of thermodynamically coherent sequences of fundamental particles that correspond to (meta)stable phases inferred from previous solubility experiments (Aja et al. 1991; Aja 1991; Yates and Rosenberg 1996).

Formation of end-member illite

Results of the present study, in conjunction with results of previous hydrothermal experiments (Aja et al. 1991; Aja 1991; Yates and Rosenberg 1996), suggest a reaction toward end-member illite through the step-wise formation of solubility-controlling phases with compositions of 0.29, 0.51, 0.69, and 0.85–0.88 $K/O_{10}(OH)_2$. Because the prograde illitization reaction indicated by these studies proceeds in only one direction (smectite$\rightarrow$illite), it represents a steady-state approach to end-member illite and, thus, the end point of the reaction is not clearly defined.

In the study by Yates and Rosenberg (1997), ATEM was used to show that bulk-grain muscovite compositions changed from 0.97(4) to 0.88(5) $K/O_{10}(OH)_2$ in hydrothermal experiments at 100° to 250 °C (including the experiments reported in the present study). Because these analyses excluded muscovite grain edges, they represent the compositions of the muscovite grain interiors. Yates and Rosenberg (1997) concluded that muscovite undergoes a retrograde reaction to form a muscovite solid solution compositionally identical to end-member illite. Because the products of these experiments retained the polytype of the starting material, $2M_1$, they are also structurally similar to end-member illites that possess the $2M_1$ polytype (e.g., Kaube illite, Środoń and Eberl 1984).

The changes in bulk grain compositions (Yates and Rosenberg 1997) and the compositional changes exhibited by the synthetic illites in the present study, suggest that the equilibration of muscovite at 250 °C may be described by two reaction paths (Fig. 9). It may be assumed that the initial dissolution of muscovite in the experiments resulted in the supersaturation of K^+, H^+, and H_4SiO_4 in solution with respect to end-member illite. The ATEM analyses of Experiment 3219, however, suggest that low-
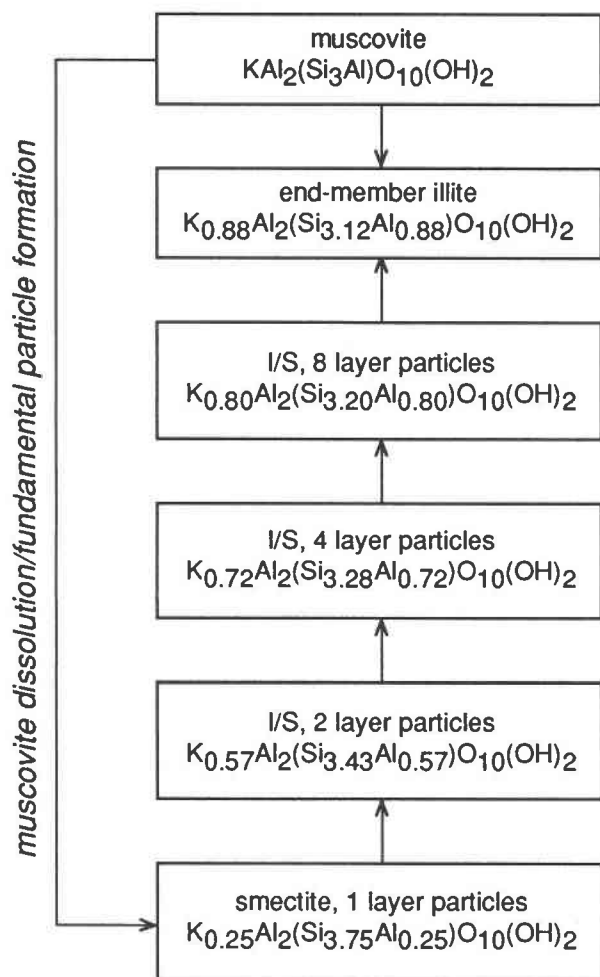
muscovite
$KAl_2(Si_3Al)O_{10}(OH)_2$

↓

end-member illite
$K_{0.88}Al_2(Si_{3.12}Al_{0.88})O_{10}(OH)_2$

↑

I/S, 8 layer particles
$K_{0.80}Al_2(Si_{3.20}Al_{0.80})O_{10}(OH)_2$

↑

I/S, 4 layer particles
$K_{0.72}Al_2(Si_{3.28}Al_{0.72})O_{10}(OH)_2$

↑

I/S, 2 layer particles
$K_{0.57}Al_2(Si_{3.43}Al_{0.57})O_{10}(OH)_2$

↑

smectite, 1 layer particles
$K_{0.25}Al_2(Si_{3.75}Al_{0.25})O_{10}(OH)_2$

muscovite dissolution/fundamental particle formation

FIGURE 9. Flow diagram showing prograde and retrograde reactions leading to the formation of end-member illite in hydrothermal Experiments at 250 °C. Fundamental particle thicknesses and calculated compositions are indicated for each of the reaction steps (see Fig. 8). Muscovite and end-member illite are assumed to consist of infinitely thick fundamental particles.

K illites are kinetically favored and represent the initial mica-like phase in the experiments. With increased experiment duration, these illites are transformed, by a process of thickening of fundamental particles related to Ostwald ripening (Eberl and Środoń 1988), through thicknesses of 2, 4, and ≥8 layers resulting in the formation of end-member illite. This mechanism is in agreement with the multiphase model (Rosenberg et al. 1990), which proposed that the step-wise reaction of mica-like phases may proceed from an initial, kinetically favored phase according to Ostwald's Step Rule.

Concurrent with the prograde formation of illites on muscovite grain edges, muscovite grain interiors changed in composition to 0.88 $K/O_{10}(OH)_2$ (Yates and Rosenberg 1997), a composition identical to that of the end point of the prograde reaction. Thus, both the prograde illitization of low-K illites and the retrograde solid solution reaction

result in the formation of end-member illite, suggesting that end-member illite is stable with respect to I/S and muscovite at 250 °C. Furthermore, these experiments were conducted with solution compositions corresponding to the stability field defined for end-member illite [0.88 $K/O_{10}(OH)_2$] at 250 °C by Yates and Rosenberg (1996). The formation of a mica-like phase with a composition of 0.88 $K/O_{10}(OH)_2$ in solutions corresponding to the stability field for end-member illite further demonstrates the stability of end-member illite in the system $K_2O-Al_2O_3-SiO_2-H_2O$ at 250 °C.

REFERENCES CITED

Ahn, J.H. and Buseck, P.R. (1990) Layer-stacking sequences and structural disorder in mixed-layer illite/smectite: Image simulations and HRTEM imaging. American Mineralogist, 75, 267–275.

Ahn, J.H. and Peacor, D.R. (1989) Illite/smectite from Gulf Coast shales: A reappraisal of transmission electron microscope images. Clays and Clay Minerals, 37, 542–546.

Aja, S.U. (1991) Illite equilibria in solution: III. A reinterpretation of the data of Sass et al. (1987). Geochimica et Cosmochimica Acta, 55, 3431–3435.

Aja, S.U., Rosenberg, P.E., and Kittrick, J.A. (1991) Illite equilibria in solutions: I. Phase relationships in the system $K_2O-Al_2O_3-SiO_2-H_2O$ between 25 and 250 °C. Geochimica et Cosmochimica Acta, 55, 1353–1364.

Bailey, S.W. (1984) Classification and structures of the true micas. In Mineralogical Society of America Reviews in Mineralogy, 13, 1–12.

Cliff, G. and Lorimer, G.W. (1975) The quantitative analysis of thin specimens. Journal of Microscopy, 103, 203–207.

Dong, H., Peacor, D.R., and Freed, R.L. (1997) Phase relations among smectite, R1 illite-smectite, and illite. American Mineralogist, 82, 379–391.

Eberl, D.D. (1993) Three zones for illite formation during burial diagenesis and metamorphism. Clays and Clay Minerals, 41, 26–37.

Eberl, D.D. and Środoń, J. (1988) Ostwald ripening and interparticle-diffraction effects for illite crystals. American Mineralogist, 73, 1335–1345.

Eberl, D.D., Środoń, J., Lee, M., Nadeau, P.H., and Northrop, H.R. (1987) Sericite from the Silverton caldera, Colorado: Correlation among structure, composition, origin, and particle thickness. American Mineralogist, 72, 914–934.

Guthrie, G.D. and Veblen, D.R. (1989) High-resolution transmission electron microscopy of mixed-layer illite/smectite: computer simulations. Clays and Clay Minerals, 37, 1–11.

———(1990) Interpreting one-dimensional high-resolution transmission electron micrographs of sheet silicates by computer simulation. American Mineralogist, 75, 276–288.

Güven, N. (1972) Electron optical observations on Marblehead illite. Clays and Clay Minerals, 20, 83–88.

———(1974) Factors affecting selected area electron diffraction patterns of micas. Clays and Clay Minerals, 22, 97–106.

Inoue, A., Kohyama, N., Kitagawa, R., and Watanabe, T. (1987) Chemical and morphological evidence for the conversion of smectite to illite. Clays and Clay Minerals, 35, 111–120.

Jasmund, K., Riedel, D., and Keddeins, H. (1969) Neubildung von Leistenformigem Illit und von Dickit bei der Zersetzung des Muscovits in

Sandstein. Proceedings of the International Clay Conference, Tokyo, 1, 493–500.

Jiang, W., Essene, E.J., and Peacor, D.R. (1990) Transmission electron microscopic study of coexisting pyrophyllite and muscovite: direct evidence for the metastability of illite. Clays and Clay Minerals, 38, 225–240.

Klimentidis, R.E. and Mackinnon, I.D.R. (1986) High-resolution imaging of ordered mixed-layer clays. Clays and Clay Minerals, 34, 155–164.

Lee, S.Y., Jackson, M.L., and Brown, J.L. (1975) Micaceous occlusion in kaolinite observed by ultramicrotomy and high resolution electron microscopy. Clays and Clay Minerals, 23, 125–129.

Moore, D.M. and Reynolds, R.C. Jr. (1989) X-ray Diffraction and the Identification and Analysis of Clay Minerals, 332 p. Oxford, New York.

Nadeau, P.H., Tait, J.M., McHardy, W.J., and Wilson, M.J. (1984a) Interstratified XRD characteristics of physical mixtures of elementary clay particles. Clay Minerals, 19, 67–76.

Nadeau, P.H., Wilson, M.J., McHardy, W.J., and Tait, J.M. (1984b) Interparticle diffraction: A new concept for interstratified clays. Clay Minerals, 19, 757–769.

———(1984c) Interstratified clays as fundamental particles. Science, 225, 923–925.

Peacor, D.R. (1992) Analytical electron microscopy: X-ray analysis. In Mineralogical Society of America Reviews in Mineralogy, 27, 113–140.

Rosenberg, P.E., Kittrick, J.A., and Aja, S.U. (1990) Mixed-layer illite/smectite: A multiphase model. American Mineralogist, 75, 1182–1185.

Ruehlicke, G. and Kohler, E.E. (1981) A simplified procedure for determining layer charge by the N-alkylammonium method. Clay Minerals, 16, 305–307.

Spence, J.C.H. (1981) Experimental High-Resolution Electron Microscopy, 370p. Oxford University Press, New York.

Środoń, J. (1980) Precise identification of illite/smectite interstratifications by X-ray powder diffraction. Clays and Clay Minerals, 28, 401–411.

Środoń, J. and Eberl, D.D. (1984) Illite. In Mineralogical Society of America Reviews in Mineralogy, 13, 495–544.

VanDerPluijm, B.A., Lee, J.H., and Peacor, D.R. (1988) Analytical electron microscopy and the problem of potassium diffusion. Clays and Clay Minerals, 36, 498–504.

Veblen, D.R., Guthrie, G.D. Jr., Livi, K.J.T., and Reynolds, R.C. (1990) High-resolution transmission electron microscopy and electron diffraction of mixed-layer illite/smectite: Experimental results. Clays and Clay Minerals, 38, 1–13.

Walther, J.V. and Helgeson, H.C. (1977) Calculation of the thermodynamic properties of aqueous silica and the solubility of quartz and its' polymorphs at high pressures and temperatures. American Journal of Science, 277, 1315–1351.

Yates, D.M. (1993) Experimental Investigation of the Formation and Stability of End-Member Illite from 100° to 250 °C and P_{v,H_2O}, 227 p. Ph.D. thesis, Washington State University, Pullman, Washington.

Yates, D.M. and Rosenberg, P.E. (1996) Formation and stability of end-member illite: I. Solution equilibration experiments at 100° to 150 °C and $P_{v,soln}$. Geochimica et Cosmochimica Acta, 60, 1873–1883.

———(1997) Formation and stability of end-member illite: II. Solid equilibration experiments at 100° to 250 °C and $P_{v,soln}$. Geochimica et Cosmochimica Acta, 61, 3135–3144.